Chinese Chemical Letters 36 (2025) 109740

Contents lists available at ScienceDirect

Chinese Chemical Letters

journal homepage: www.elsevier.com/locate/cclet

Mixed-anion square-pyramid [SbS_3I_2] units causing strong second-harmonic generation intensity and large birefringence

Yu Zhou [a,c], Lin-Tao Jiang [a,c], Xiao-Ming Jiang [a,b], Bin-Wen Liu [a,b,*], Guo-Cong Guo [a,b,*]

[a] State Key Laboratory of Structural Chemistry, Fujian Institute of Research on the Structure of Matter, Chinese Academy of Sciences, Fuzhou 350002, China
[b] Fujian Science & Technology Innovation Laboratory for Optoelectronic Information of China, Fuzhou 350002, China
[c] College of Chemistry, Fuzhou University, Fuzhou 350116, China

ARTICLE INFO

Article history:
Received 19 January 2024
Revised 27 February 2024
Accepted 6 March 2024
Available online 8 March 2024

Keywords:
Chalcohalide
Mixed-anionic units
Nonlinear optical
Birefringence
Structure-property relationship

ABSTRACT

Enhancement of the nonlinear optical (NLO) output power of lasers requires urgent development of an NLO crystal with a significant second-harmonic generation (SHG) response and sufficient birefringence for phase-matching capability; however, simultaneously optimizing these two key parameters remains a great challenge. In contrast to traditional single-anion units, the stereochemically-active lone pair Sb^{3+} ion is coordinated by S^{2-} and I^- ions to yield the mixed-anionic SbSI chalcohalide that can enhance hyperpolarizability and anisotropic polarizability concurrently. As anticipated, SbSI exhibited the largest SHG response ($5.7 \times AgGaS_2$@1.91 μm) among phase-matching Sb-based sulfides, the favorable laser-induced damage threshold (LIDT, $2.3 \times AgGaS_2$@2.09 μm), and the giant calculated birefringence (0.62@1.91 μm). Structural analysis and computational simulations indicate that the highly polarizable mixed anion determine the enormous SHG response and birefringence.

Second-order mid- and far-infrared (IR) NLO crystals that play a crucial role in solid-state lasers generate of output spectral ranges previously inaccessible in various fields, such as medical treatment, information storage, laser guidance, and precision micromanufacturing [1–7]. An exceptional IR NLO material must meet several critical prerequisites: (1) Exhibiting a significant SHG effect to ensure optimal laser conversion efficiency; (2) Possessing sufficient birefringence to achieve phase-matching behavior; (3) Having a broad transparency absorption cut-off edge that is necessary to cover key atmospheric windows; (4) Displaying the high laser-induced damage threshold that is crucial to enhance resistance against high-energy laser damage; (5) Showing excellent physicochemical stability [8–11]. Among these optical demands, designing NLO materials with considerable NLO efficiency is a fundamental and urgent topic that has driven continuous exploration. Meanwhile, numerous NLO crystals display strong SHG intensities but lack phase-matching capability at specific transparency windows, which seriously restricts and hinders their further application. An example of such compounds was $Ba_3AGa_5Se_{10}Cl_2$ (A = Cs, Rb, K), where the alignment parallel of the Ga_5Se_{10} anionic group primarily contributed to the impressive NLO coefficient but suffered from tiny birefringence due to the nearly isotropic polyhedrons of the tetrahedral units [12]. Therefore, the presence of favorable SHG intensity and significant birefringence for phase-matching capability are two crucial factors that significantly contribute to the advancement of NLO materials.

In essence, the macroscopic performance of NLO materials is determined by their microstructure. Several design strategies have been traditionally employed to address the challenge of achieving large NLO coefficients and sufficient birefringence. These strategies include incorporating of the Jahn-Teller effect or stereochemically-active lone pairs centered polyhedra, as well as π-π interacting plane triangles [13–17]. We refer to these polyhedrons, where one central atom is bonded by the same anions, as single-anion basic building units. In contrast to traditional single-anion units, mixed-anion units exhibit larger distorted polyhedrons due to the varying sizes and electronegativities of the anions, which possess stronger hyperpolarizability and polarizability anisotropy, offering fascinating possibilities for impressive NLO responses and benefiting phase-matching behavior. These NLO functional motifs make mixed-anion basic building units favorable configurations for producing outstanding NLO materials [18]. For instance, in the ultraviolet-visible region, introducing fluorine elements into oxides to yield fluorooxoborates has been reported as a vital constituent in borate-based structural chemistry. This approach has been created highly distorted tetrahedral BO_3F units, leading to extra-large SHG and sufficient birefringence [19]. However, in the mid- and far-IR regions, only a few cases of IR NLO materials have been

* Corresponding authors.
E-mail addresses: bwliu@fjirsm.ac.cn (B.-W. Liu), gcguo@fjirsm.ac.cn (G.-C. Guo).

https://doi.org/10.1016/j.cclet.2024.109740
1001-8417/

conducted due to synthetic difficulties of chalcogenides or phosphides. For example, the incorporation of fluorine elements into Na_3SiS_3F chalcohalide generated a significant degree of distortion in the tetrahedral SiS_3F unit, making it to the benefit of displaying moderate SHG response and large birefringence [20]. Therefore, the use of mixed-anion polyhedral units in IR NLO materials to enhance the SHG response and birefringence is rarely researched, but it is incredibly urgent.

The Sb^{3+} ion, coordinated by several chalcogenides Q (Q = S, Se, Te) atoms gave rise to the molecular geometries of trigonal pyramidal SbQ_3, seesaw SbQ_4, and square-pyramidal SbQ_5 units, often resulting in chalcogenides with excellent properties [21–24]. For mixed-anion units, the double-cubane compound $[Sb_7S_8Br_2](AlCl_4)_3$, which displayed an SHG signal, has been synthesized using an ionic liquid method [25]. These SHG-active results constantly inspire us to incorporate halide atoms into the SbQ_x (x = 3–5) units, which not only ensures structural diversity but also optimizes the NLO properties by introducing intrinsic polarization anisotropy and hyperpolarizability. According to the above ideas, by combining stereochemically-active lone pair Sb^{3+} ions with mixed-anionic S^{2-} and I^- ions with different sizes, a square-pyramidal unit was created, resulting in a mixed-anionic chalcohalide called SbSI. Previous reports have mainly focused on its notable ferroelectric characteristics, but the investigation of its second-order NLO properties has not been reported [26,27]. As a result, the highly hyperpolarizable and polarizable square-pyramidal structure of SbSI enabled it to possess the strong SHG response, the favorable laser-induced damage threshold, and exceptionally large calculated birefringence.

After conducting a comprehensive literature review, various synthesis methods have been discovered for preparing polycrystalline SbSI, including hydrothermal, chemical vapor transport, and sonochemical synthesis [27–29]. In addition to these methods, two additional synthesis approaches were employed to synthesize the desired crystal: (1) Combining the raw materials Sb (1.0 mmol), S (1.0 mmol), and I_2 (0.5 mmol) in a solid-state reaction at 450 °C; (2) Blending the reactant Sb_2S_3 (1.0 mmol) and NaI (2.0 mmol) through a solid-state reaction at 700 °C (see Supporting information). The crystal SbSI possessed physicochemical stability in air and water for six months at room temperature without any appearance or weight loss changes. To ensure the exact composition of SbSI, the energy dispersive X-ray spectroscopy (EDS) verified the presence of Sb, S, and I elements (Fig. S1 in Supporting information). The experimental powder X-ray diffraction (XRD) patterns of SbSI closely matched the simulated patterns, indicating its high purity (Fig. S2 in Supporting information). Furthermore, the IR transmission range of SbSI, without any absorption peaks related to chemical bonds within the range of 4000 cm^{-1} to 400 cm^{-1}, marked it a potential candidate for optical applications in the mid- and far-IR regions (Fig. S3 in Supporting information). The UV–vis–NIR diffuse reflectance spectrum of SbSI demonstrated a steep absorption edge at 1.94 eV (Fig. S4 in Supporting information), which correlated with its red color.

The crystal structure of SbSI adopts a noncentrosymmetric and polar orthorhombic space group $Pna2_1$ at the temperature of 280 K. It is composed of one-dimensional chains formed by infinite $[Sb_2S_4I_2]^{4-}$ chains that run along the c-axis (Fig. 1a). Each chain consists of two identical square pyramids $[SbS_3I_2]^{5-}$ units by edged-sharing S atoms (Fig. 1b). The Sb atom is coordinated by three S and two I atoms, with Sb-S (Sb-I) bond distances of 2.467–2.795 Å (3.012–3.234 Å) and S-Sb-S (I-Sb-I) bond angles ranging from 82.58° to 98.87° (equaling 82.18°). Additionally, while the local dipole moment of SbSI possesses a net orientation that equals zero running along the a- and b-axes, it is 4.00 Debye along the c-axis, giving it polar characteristic [30].

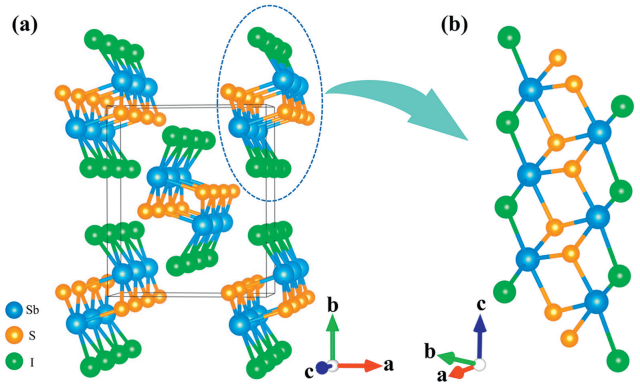

Fig. 1. (a) Crystal structure of SbSI is consisted of one-dimensional $[Sb_2S_4I_2]^{4-}$ chains. (b) The separate $[Sb_2S_4I_2]^{4-}$ chain is built of $[SbS_3I_2]^{5-}$ units.

Being a noncentrosymmetric crystal, SbSI has the SHG activity. The SHG response of SbSI was evaluated using a modified Kurtz-Perry method [31], with the reference material being optical purity $AgGaS_2$ (AGS). The particle sizes of both SbSI and AGS were varied within five dimensions, namely 30–50, 50–75, 75–100, 100–150, and 150–200 μm (microcrystals SbSI were prepared through the above synthesis method 2). Under an incident laser wavelength of 1910 nm, the SHG signal of SbSI was observed at 955 nm (Fig. 2a). The SHG intensities of SbSI increased with larger particle sizes, indicating type I phase-matching behavior. When comparing the SHG intensities of SbSI with AGS at a particle size of 150–200 μm, it was found that SbSI exhibited a significantly higher SHG response, approximately 5.7 times greater than that of AGS (Fig. 2b). When compared to other Sb-based NLO sulfides (Fig. 2c), SbSI represented the highest SHG intensity among phase-matching Sb-based sulfides.

To investigate optical properties induced by the I atom in the $[SbS_3I_2]$ square pyramid, the hyperpolarizability of structural units in Sb_2S_3, SbSBr, and SbSI [32,33] was examined using the Gaussian 09 package with the PBE1PBE functional method and def2TZVP basis set [34,35]. The calculated hyperpolarizability of the structural unit in SbSI was found to be higher than that in SbSBr and Sb_2S_3 (Fig. 2d). This enhancement in hyperpolarizability was attributed to the introduction of an I atom, which created the mixed anionic tetragonal $[SbS_3I_2]$ unit, leading to a significant increase in the SHG intensity. Moreover, according to the NLO functional motifs, the structural units of an NLO active crystal play a vital role in determining nonlinearity [36]. The percent of $[SbS_3I_2]$ density in the unit cell of SbSI was 100% determined its own SHG effect. It is the "sole functional modules" that mainly contribute to the large SHG intensity [37]. Additionally, the contributions of atomic orbital-resolved d_{15}, d_{24}, and d_{33} tensors in SbSI were also computed to gain further insight into the NLO functional motifs. As depicted in Fig. 2e, the theoretical NLO contribution rates of the Sb, S, and I atoms were found to be 30%, 21%, and 49%, respectively. Furthermore, SbSI possessed three nonzero independent SHG coefficient tensors (d_{15}, d_{24}, and d_{33}) under the constraint of Kleinman's symmetry. The calculated SHG tensors for SbSI were displayed in Fig. 2f. At an incident laser wavelength of 1910 nm (equivalent to 0.65 eV), the d_{15}, d_{24}, and d_{33} values for SbSI were determined as 8.9, −71.6, and −134.1 pm/V, respectively. The effective NLO coefficient (d_{eff}) of SbSI at 1910 nm was calculated as 79.5 pm/V based on the modified Kurtz-Perry method, using $d_{eff,AGS}$ = 11.6 pm/V as a reference.

The LIDT of SbSI was determined using the single-pulse LIDT method [38]. The results, presented in Table S5 (Supporting information), showed that SbSI disclosed a single-crystal LIDT value of 20.8 MW/cm^2, which was approximately 2.3 times higher than

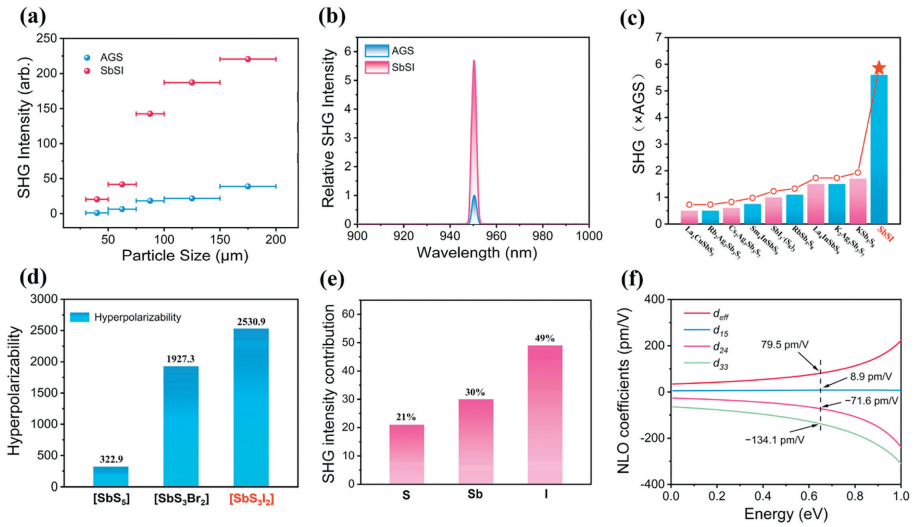

Fig. 2. (a) Phase-matching behaviors of SbSI and AGS at the incident laser of 1910 nm. (b) SHG signals of SbSI and AGS in the 150−200 μm particle size. (c) Comparison of SHG intensities in SbSI and other phase-matching Sb based NLO sulfides. (d) The calculated hyperpolarizability of structural units in Sb_2S_3, SbSBr, and SbSI. (e) Calculated atom SHG response contributions. (f) Calculated NLO coefficients of SbSI.

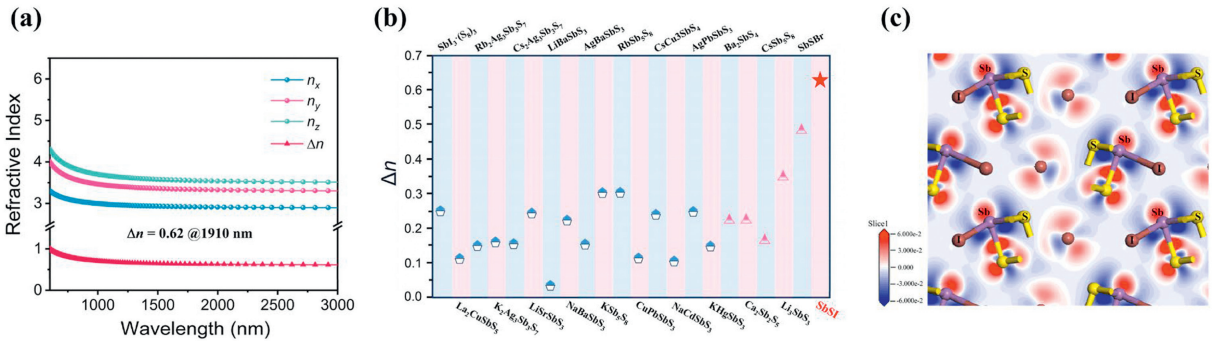

Fig. 3. (a) Calculated refractive indices and birefringence of SbSI. (b) Comparison of birefringence between SbSI and several Sb-based sulfides. (c) Electron-density difference map of SbSI.

that of the optical purity wafer AGS (9.0 MW/cm^2) when exposed to a laser beam of 2090 nm. The laser damage of NLO material is unclear and can be influenced by various factors, such as band gap, thermal expansion coefficient, thermal conductivity, and crystal defects [39]. In the case of SbSI, it has an optical band gap of 1.94 eV, which mitigates two-photon absorption at the incident laser wavelength of 2090 nm. Additionally, thermal properties also play a crucial role in determining the LIDT. The linear thermal expansion coefficient (α_L) of SbSI along the *a*-, *b*-, and *c*-axes was shown in Fig. S5 (Supporting information), with values of 2.12×10^{-5}, 3.01×10^{-5}, and -2.01×10^{-5}, respectively. The high thermal expansion anisotropy (TEA) value is attributed to the presence of a negative thermal expansion coefficient in α_L. While the lattice constants *a* and *b* exhibited a nonlinear increase with rising temperatures, the lattice constant *c* decreased within the temperature range from 100 K to 280 K. Such a phenomenon was consistent with the attributes of AGS, where the negative α_c value was attributed to the vibrations of Ag and Ga atoms in low-frequency transverse modes [40]. The TEA of SbSI was estimated to be 2.49, slightly lower than that of AGS (2.95) [41]. Noted that the LIDT often shows a positive correlation with the band gap and a negative association with TEA in chalcogenides. Therefore, when exposed to high-power laser irradiation, SbSI exhibited enhanced resistance to thermal shock possible due to the reduced TEA.

The refractive indexes of SbSI were calculated by the *ABINIT* package, as illustrated in Fig. 3a. Among the indices along different directions, n_z and n_x represent the largest and smallest refractive indices, respectively. The refractive index dispersion of SbSI demonstrated strong anisotropy, with a significant birefringence ($\Delta n = 0.62$) at 1.91 μm. The analysis of the electron density difference of SbSI on the plane (Fig. 3c) revealed visible asymmetric lobes around the Sb atoms, indicating that the lone pair electrons on Sb atoms contributed to the optical anisotropy and increased birefringence. According to the type I phase-matching condition of $n_e(\omega) = n_o(2\omega)$, where ω and 2ω represent the fundamental and second-harmonic light, respectively, the phase-matching cut-off wavelength of SbSI was 0.52 μm (Fig. S6 in Supporting information), which aligned with the experimental phase-matching behavior at the incident laser wavelength of 1.91 μm. These results confirmed the effectiveness of incorporating the tetragonal pyramid structure to enhance the birefringence of crystals. To further validate the superiority of the tetragonal pyramid structure, we conducted a search in the Inorganic Crystal Structure Database (ICSD) to identify the Sb-based sulfides. The results clearly demonstrated that SbSI displayed significantly larger birefringence performance compared to other Sb-based sulfides (Fig. 3b), establishing itself as having the highest level of birefringence among Sb-containing sulfides.

In summary, to acquire an NLO material with a strong NLO effect and sufficient birefringence, the stereochemically-active lone pairs Sb^{3+} ion was coordinated by mixed-anion with enhancing hyperpolarizability and anisotropic polarizability. As anticipated, SbSI was successfully synthesized and exhibited the highest SHG response (5.7 times that of AGS) among phase-matching Sb-based

sulfides, the satisfactory LIDT and the giant calculated birefringence (0.62@1.91 μm) for ensuring phase-matching. This work suggests that the mixed anion square-pyramid structure can be considered an ideal basic structural unit for designing NLO materials with favorable SHG coefficients and large birefringence.

Declaration of competing interests

The authors declare that they have no known competing financial interests or personal relationships that could have appeared to influence the work reported in this paper.

Acknowledgments

This work was supported by the National Natural Science Foundation of China (Nos. 21921001, 22075283, 92161125, 22175172, 21827813, U21A20508), the Youth Innovation Promotion Association of Chinese Academy of Sciences (Nos. 2020303, 2021300), and the Fujian Science & Technology Innovation Laboratory for Optoelectronic Information of China (No. 2020ZZ108).

Supplementary materials

Supplementary material associated with this article can be found, in the online version, at doi:10.1016/j.cclet.2024.109740.

References

[1] M. Mutailipu, J. Han, Z. Li, et al., Nat. Photonics 17 (2023) 694–701.
[2] J. Zhang, C. Wu, H. Shi, et al., Matter 6 (2023) 1188–1202.
[3] X. Huang, S.H. Yang, X.H. Li, et al., Angew. Chem. Int. Ed. 61 (2022) e202206791.
[4] C. Jiang, X. Jiang, C. Wu, et al., J. Am. Chem. Soc. 144 (2022) 20394–20399.
[5] M. Wu, E. Tikhonov, A. Tudi, et al., Adv. Mater. 35 (2023) 2300848.
[6] Y. Chu, H. Wang, T. Abutukadi, et al., Small 19 (2023) 2305074.
[7] X. Dong, L. Huang, H. Zeng, et al., Angew. Chem. Int. Ed. 134 (2022) e202116790.
[8] Q. Wu, L. Kang, Z. Lin, Adv. Mater. 36 (2024) 2309675.
[9] Y.Y. Li, W.J. Wang, H. Wang, et al., Cryst. Growth Des. 19 (2019) 4172–4192.
[10] S. Yang, C. Lin, H. Fan, et al., Angew. Chem. Int. Ed. 62 (2023) e202218272.
[11] C. Wu, C. Jiang, G. Wei, et al., J. Am. Chem. Soc. 145 (2023) 3040–3046.
[12] P. Yu, L.J. Zhou, L. Chen, J. Am. Chem. Soc. 134 (2012) 2227–2235.
[13] S. Han, A. Tudi, W. Zhang, et al., Angew. Chem. Int. Ed. 62 (2023) e202302025.
[14] Y. Liu, X. Liu, S. Liu, et al., Angew. Chem. Int. Ed. 59 (2020) 7793–7796.
[15] Y. Hu, C. Wu, X. Jiang, et al., Angew. Chem. Int. Ed. 62 (2023) e202315133.
[16] J. Huang, S. Guo, Z. Zhang, et al., Sci. China Mater. 62 (2019) 1798–1806.
[17] Y. Huang, Y. Zhang, D. Chu, et al., Chem. Mater. 35 (2023) 4556–4563.
[18] W.K. Wang, D.J. Mei, S.G. Wen, et al., Chin. Chem. Lett. 33 (2022) 2301–2315.
[19] B. Zhang, G. Shi, Z. Yang, et al., Angew. Chem. Int. Ed. 56 (2017) 3916–3919.
[20] J. Zhou, L. Wang, Y. Chu, et al., Adv. Opt. Mater. 11 (2023) 2300736.
[21] H.J. Zhao, Y.F. Zhang, L. Chen, J. Am. Chem. Soc. 134 (2012) 1993–1995.
[22] M.C. Chen, L.M. Wu, H. Lin, et al., J. Am. Chem. Soc. 134 (2012) 6058–6060.
[23] W. Yin, M. Zhou, A.K. Iyer, et al., J. Alloys Compd. 729 (2017) 150–155.
[24] W. Hao, D. Mei, W. Yin, et al., J. Solid State Chem. 198 (2013) 81–86.
[25] Q. Zhang, I. Chung, J.I. Jang, et al., J. Am. Chem. Soc. 131 (2009) 9896–9897.
[26] M. Balkanski, M.K. Teng, M. Massot, H. Bilz, Ferroelectrics 26 (2011) 737–741.
[27] C. Wang, S. Xiao, X. Xiao, et al., J. Phys. Chem. C 125 (2021) 15441–15447.
[28] P. Szperlich, B. Toroń, M. Nowak, et al., Mater. Sci. Pol. 32 (2014) 669–675.
[29] R.Žaltauskas Audzijonis, R. Sereika, et al., Phase Transit. 90 (2016) 312–316.
[30] J.H. Wu, C.L. Hu, T.K. Jiang, et al., J. Am. Chem. Soc. 145 (2023) 24416–24424.
[31] S.K. Kurtz, T.T. Perry, J. Appl. Phys. 39 (1968) 3798–3813.
[32] T.J. Inushima, Phys. Chem. Solids 60 (1999) 587–598.
[33] R.J.D. Tilley, A.C. Wright, J. Solid State Chem. 64 (1986) 1–21.
[34] J. Xu, Y. Xiao, K. Wu, et al., Small 20 (2024) 2306577.
[35] T. Lu, F.W. Chen, J. Comput. Chem. 33 (2012) 580–592.
[36] K. Feng, L. Kang, Z. Lin, et al., J. Mater. Chem. C 2 (2014) 4590–4596.
[37] C. Jin, X. Jiang, C. Wu, et al., Angew. Chem. Int. Ed. 62 (2023) e202310835.
[38] M.J. Zhang, X.M. Jiang, L.J. Zhou, G.C. Guo, J. Mater. Chem. C 1 (2013) 4754–4760.
[39] S.F. Li, X.M. Jiang, Y.H. Fan, et al., Chem. Sci. 9 (2018) 5700–5708.
[40] J. Wu, W. Huang, H.G. Liu, et al., Cryst. Growth Des. 20 (2020) 3140–3153.
[41] B.W. Liu, H.Y. Zeng, X.M. Jiang, G.C. Guo, CCS Chem. 3 (2020) 964–973.